


Ultrasonic and Nanoindentation Evaluation of SAF 2507 Aging: Elastic Moduli, Attenuation, and Microstructure

Brenno Lavigne Diniz^{a,*} , Ygor Tadeu Bispo dos Santos^a, Virginia Ribeiro dos Santos^a,
Ísis Moraes Cruz Souza Fernandes^a, Ariane Cândido Batista^a, Luiz Antonio Pimentel Cavalcanti^a,
Ivan Costa da Silva^a

^aInstituto Federal de Educação, Ciência e Tecnologia da Bahia, Grupo de Pesquisa em Ensaios
Não Destrutivos (GPEND), Salvador, BA, Brasil.

Received: February 28, 2024; Revised: July 13, 2024; Accepted: July 18, 2024

Super duplex stainless steels are highly recommended for corrosive environments. However, detrimental phases tend to precipitate in the austenite-ferrite interfaces at certain temperatures. In this study, the elastic moduli of ten specimens of SAF 2507 that underwent isothermal heat treatment at 900 °C for different amounts of time were determined using the ultrasonic non-destructive technique. These results were validated by nanoindentation, confirming the accuracy of the ultrasonic inspection. An investigation of microstructural changes, employing optical microscopy and X-ray diffraction, enabled elucidation of how these modifications influence acoustic wave attenuation and velocity, as well as the elastic modulus. As the ferrite content decreases and the sigma phase content increases, the attenuation coefficients tend to decay, while the elastic modulus increases until a treatment time of 45 min and remains stable for higher aging times. Additionally, a robust correlation between shear wave velocity and the elastic modulus was identified.

Keywords: *Super duplex, nondestructive testing, nanoindentation, ultrasonics, metallography.*

1. Introduction

Super duplex stainless steel (SDSS) SAF 2507 is a metallic alloy comprised of nearly equal proportions of ferrite (δ) and austenite (γ) phases¹ that finds numerous applications in the petrochemical field and other industries². It exhibits outstanding mechanical and corrosion properties because of its microstructure – i.e., excellent resistance to intergranular and fatigue corrosion due to the austenite phase and increased toughness and elastic modulus due to the ferrite phase. Nevertheless, deleterious intermetallic phases, such as sigma (σ), chi (χ), and others, are generated during thermal treatment and aging of SAF 2507 and a range of similar steel alloys^{3,4}. These secondary phases negatively affect mechanical and corrosion properties and may compromise material performance in general applications. Among these deleterious secondary phases that precipitate in the intergranular boundaries of SDSS alloys, the sigma phase is the most deleterious one as it causes significant drops in mechanical strength and corrosion resistance⁵.

Recent advancements in the metallurgy of duplex stainless steels (DSSs) have been made over the past years, with new studies offering significant insights into the corrosion resistance and microstructural stability of this class of materials. For instance, one study explored the corrosion resistance of DSSs in the context of gas metal arc welding (GMAW), highlighting the impact of welding parameters on

phase balance and corrosion properties⁶. Another research investigated the influence of electropulsing treatments on the mechanical properties of UNS S32750 DSS and found that this procedure led to an increase in fracture strain compared to reference tests and a decrease in microhardness, improving the material's mechanical response. Thus, this method proved useful in optimizing material performance without the need for extensive post-processing treatments, such as annealing in a dedicated furnace⁷. Another study characterized the microstructure and corrosion behavior of welded joints between SDSS SAF 2507 and low alloy steel E690, highlighting significant microstructural changes, element diffusion, and localized corrosion that increase stress corrosion cracking vulnerability⁸.

Notably, the sigma phase predominantly affects the ferritic matrix of SDSSs, as its diffusion rates in ferrite are approximately one hundred times higher than in austenite⁹. The sigma phase, also found in DSSs, has a tetragonal crystalline structure, and is an intermetallic constituent composed mainly of chromium (~30%), molybdenum (~7%), and nickel (~4%)¹⁰. As the precipitation of sigma advances, Cr and Mo tend to migrate to this phase, which leads to a decrease of these elements in ferrite, especially Mo. The sigma phase starts to form in the intergranular boundaries between ferrite and austenite, where initial nucleation occurs; later, it grows inside the ferritic grains. Molybdenum plays a crucial role in the precipitation of this secondary phase.

*e-mail: brennolavdin@gmail.com

The other relevant secondary phase is chi, which has a body-centered cubic structure, and contains roughly 25% Cr, 14% Mo, and 3% Ni. It starts forming at the same temperatures as sigma, albeit in significantly lower contents¹⁰. The chi phase has an even higher Mo content than that of sigma. Its nucleation process starts during the last phase of aging, due to the characteristically low energy in the chi/ferrite interface, which is highly coherent and the relationship between the crystalline orientations is cubic to cubic^{11,12}. The ferrite gives rise to secondary phases, such as sigma and chi, through a eutectoid reaction, as represented in Equation 1.



The chi phase is the first to precipitate, although sigma is more stable thermodynamically¹³, and after a prolonged aging time the chi phase turns into sigma¹⁴. It is important to note that DSSs generally contain nitrogen in a content of up to 0.5% in weight. The addition of N serves the purpose of increasing material strength and resistance to pitting corrosion. Chromium-nitride (Cr_2N), which has a hexagonal structure, might arise in DSSs with higher N contents, as well as in the fused zone during welding processes. The growth of the sigma and chi precipitates results in an additional depletion of Cr and Mo in ferrite. As a result, the ferrite regions with high Ni content become unstable and eventually give rise to secondary austenite¹¹. The sigma phase is subject of special interest in the study of DSSs because it may cause significant reductions in ductility and mechanical properties, and it increases corrosion susceptibility owing to its ability to accumulate alloying elements like Cr and Mo¹⁵⁻¹⁷.

The elastic modulus is an intrinsic material property and is an important parameter in the field of engineering, as it contains information regarding the mechanical behavior of materials. There are different ways to measure elastic constants (ASTM provides a wide range of tests for that purpose), the most common of them being a tensile test. However, the destructive nature of this testing approach can limit its practicality in industrial applications. The ultrasonic nondestructive test comes up as a viable material characterization option that can be used to determine a wide range of properties, including elastic and shear moduli, Poisson coefficients and many others¹⁸⁻²⁰. The ultrasonic test relies on the measurement of longitudinal and shear wave modes, as well as attenuation. These parameters provide insights into the elastic constants and density, revealing details about the microstructure of the material, as grain boundaries and other heterogeneities will have an impact on the dissipation of waves by means of acoustic absorption, which in turn influence the attenuation coefficient²¹⁻²³.

The incidence of ultrasonic waves in a material excites its particles, which results in mechanical vibrations that propagate in the medium in a preferential direction. This propagation can be of two different modes: longitudinal, when the wave moves by compression and rarefaction in the pulse direction, and shear/transverse, when the wave propagates by shear forces between adjacent crystallographic planes, with the direction of propagation being perpendicular to the oscillatory movement of the particles²⁴. The spread of an

ultrasonic pulse through a solid material causes temporary elastic deformations and internal stresses, which propagate in the medium with a finite velocity. When propagating in crystalline materials, these pulses interact with lattice and volumetric defects, such as inclusions, cracks, and porosities^{25,26}.

When it comes to SDSS alloys, their constituent phases respond differently when subjected to ultrasonic waves. This is because the austenite phase exhibits a greater number of vibrational modes compared to ferrite^{27,28}. This difference in behavior arises from the face-centered cubic (FCC) crystalline structure of austenite, in contrast to the body-centered cubic (BCC) cell characteristic of ferrite. The increased vibrational capacity of the austenite cell facilitates easier dispersion of ultrasonic energy, leading to a higher magnitude for the attenuation coefficient when compared to the ferritic phase. Additionally, it is noteworthy that, in general, materials with higher anisotropy tend to exhibit greater attenuation. This phenomenon can be attributed to the complex interplay of various energy loss mechanisms, such as diffraction, scattering, and absorption²⁹, which are particularly pronounced in anisotropic materials.

It is desirable to validate the results found by employing the equations that correlate ultrasonic velocities and elastic constants by comparing them to data obtained in experiments. With that objective, instrumented indentation techniques can be used for determining elastic and mechanical properties of materials³⁰; among these, the nanoindentation method has been increasingly utilized to measure load and strain/displacement with high accuracy down to the nanoscale level³¹. This technique has been used to determine mechanical properties like hardness, residual stresses, and elastic constants with state-of-the-art precision^{20,32}. Studies analyzing the usage of nanoindentation for characterizing the microstructure of austenitic steels and other metallic alloys showed good applicability of this testing technique for assessing how the mechanical properties are influenced by crystalline microstructure^{30,33}. Each cycle of loading and unloading with the nanoindenter generates data points that can be plotted in a 2D chart where load is the vertical axis and displacement is the horizontal axis. These curves exhibit features that provide insights into the complex elastic and plastic deformation phenomena that take place when the tip of the indenter is pushed onto the sample's surface³⁴.

To address the challenges posed by the formation of deleterious phases during the aging of SAF 2507 SDSS, the present work aims to investigate the elastic moduli changes using both ultrasonic non-destructive testing and the nanoindentation technique. By comparing these methods, we seek to validate the accuracy of ultrasonic measurements and explore their relationship with microstructural transformations. This comprehensive approach, which includes the study of the microstructure of SAF 2507 by means of optical microscopy, scanning electron microscopy (SEM), and X-ray diffraction analyses, provides new insights into the effects of heat treatment on mechanical properties of SDSSs. This way, the present study aims to present the benefits of employing these practical techniques in the evaluation of product conformance and monitoring of equipment health, which are particularly useful aspects in the quality control

and preventive maintenance routines for industrial segments that deal with this type of stainless steel.

2. Materials and Methods

2.1. Materials

The SDSS SAF 2507 specimens were prepared from a solubilized hot forged ingot with the following chemical composition in weight: Fe - 62.00%, Cr - 24.80%, Ni - 7.11%, Mo - 3.59%, Mn - 0.93%, Si - 0.50%, Cl - 0.26%, Cu - 0.18%, V - 0.12%, C - 0.03% (max), besides other elements that are present in lower contents (e.g. P, S, and others). The composition of the received ingot was determined using a Bruker X-ray fluorescence equipment, model S2 Ranger.

2.2. Solubilization and heat treatment

In the present study, ten SAF 2507 specimens were cut from the original ingot and underwent a solubilization treatment at 1110 °C for 30 min. The dimensions of the specimens were 40 x 40 x 10 mm. Specimen S0 was kept in the solubilized condition in order to be used as a reference. The other nine specimens were exposed to a temperature of 900 °C for different amounts of time, after which they were rapidly cooled in water. The terminology of the specimens is presented in Table 1. After cooling, the specimens were prepared for measurements. The densities of the specimens were measured with a DSL910 digital densimeter using ethyl alcohol at 96% concentration.

2.3. Metallographic analysis

All specimens were ground with 220#, 320#, 400#, 600#, 1000#, and 1200# mesh sandpaper. They were then polished with alumina suspensions with the following granulometries: 1.00 µm, 0.31 µm, and 0.05 µm. The specimens were etched with Beraha's tint, with HCl p.a. at a concentration of 2.00 mol/L and 0.6 g of potassium metabisulfite p.a. The etched specimens were subsequently exposed to drying with a jet of hot air³⁵.

The optical microscope used was an Olympus CX 30. For quantifying the percentages of the sigma and ferrite phases present in each specimen, the ImageJ® software was used. As to the magnetic ferritic phase, a second independent measurement procedure was performed using a Helmut-Fischer® ferritescope model MP3, with the purpose of double-checking the percentage of this phase in each specimen.

SEM was performed on a JSM-6510LV microscope with a tungsten filament, at an acceleration voltage of 20 kV, a working distance of 12 to 15 mm, and a spot size of SS50 (arbitrary unit). The images were taken using backscattered electron (BSE) detectors in combination with the energy dispersive spectroscopy (EDS) technique, using equipment of the Thermo Scientific brand, model 6724A-1UUS-SN. The surface preparation and etching for SEM were the same as for optical microscopy.

2.4. X-ray diffractometry

The effects of heat treatment on the SDSS specimens were also investigated using x-ray diffraction (XRD). The XRD technique was used in this work to identify the phases, especially sigma, using a Shimadzu diffractometer model XRD - 7000, scanning an angular interval from 20 to 90°. CuK α radiation was used with a wavelength of 0.154 nm. The tension and current parameters were 40 kV and 30 mA, respectively. For this testing, the specimens were ground with a 600# sandpaper followed by polishing with 0.30 µm alumina suspension.

2.5. Ultrasonic inspection

The measurements of ultrasonic velocities were performed under the experimental setup shown in Figure 1, using an Olympus Panametrics® 5077PR pulse-receiver, a digital oscilloscope Tektronix® model TDS 2024B at 250 Ms/s sampling rate, a Panametrics® MB4S (2.25 MHz) longitudinal transducer, and a V154 (2.25 MHz) shear transducer. For measuring attenuation, a 4 MHz longitudinal transducer was used.

Table 1. Heat treatment times for the specimens used.

Time (min)	0	5	15	30	45	60	90	120	150	180
Specimen	S0	S5	S15	S30	S45	S60	S90	S120	S150	S180

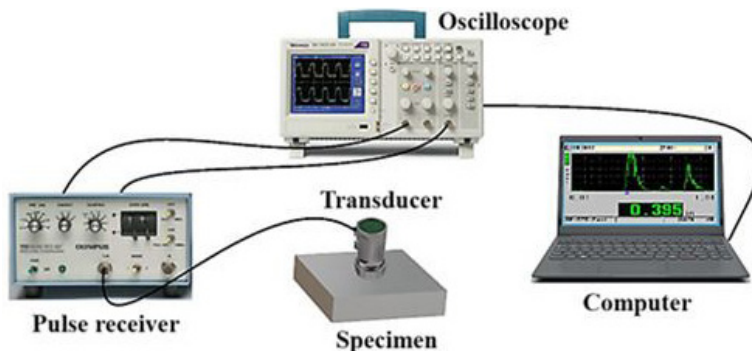


Figure 1. Experimental setup for the ultrasonic testing.

The elastic modulus E and the Poisson ratio ν can be calculated as functions of the longitudinal acoustic velocity V_L and the shear velocity V_S ^{19,20,36} through Equations 2 and 3, respectively, where ρ is the specimen's density. Both the longitudinal and shear acoustic velocities are equal to thickness divided by half round trip transit time.

$$E = V_L^2 \rho \frac{(1+\nu)(1-2\nu)}{1-\nu} \quad (2)$$

$$\nu = \frac{1-2(V_S/V_L)^2}{2-2(V_S/V_L)^2} \quad (3)$$

Denoting the peak amplitude of the first and second echo signal A_0 and A_1 , respectively, and the specimen thickness as L , the attenuation coefficient α is defined in Equation 4.

$$\alpha = \frac{20 \log(A_0/A_1)}{2L} \quad (4)$$

2.6. Nanoindentation

The indentation measurements were performed using Anton Paar's NHT³ nanoindenter (Hit 300), which can determine instrumented hardness (HIT) and instrumented elastic modulus (EIT) in a single continuous measurement with automated calculations performed on the data from the loading-unloading curve. The nanoindenter measures the unloading stiffness S , which is related to the reduced elastic modulus E_r . This reduced modulus is then used to determine the instrumented elastic modulus E . These moduli can be calculated from Equations 5 and 6, respectively, where A is the normal projection area, S is the specimen's measured unloading stiffness, and ν_i and E_i are the indenter's known Poisson coefficient and elastic modulus, respectively.

$$E_r = \frac{S}{2} \sqrt{\frac{\pi}{A}} \quad (5)$$

$$E = \frac{1-\nu^2}{E_r^{-1} - (1-\nu_i^2)E_i^{-1}} \quad (6)$$

3. Results and Discussion

3.1. Phase changes induced by heat treatment

Figure 2a depicts the X-ray diffraction spectrum of the solubilized specimen S0 at 1200 °C. This spectrum reveals distinct peaks corresponding to ferrite and austenite phases, confirming the effectiveness of the solubilization process. Figure 2b confirms the microstructural change induced by heat treatment, revealing the presence of the sigma phase

for the sample isothermally treated for 30 min. Redundant spectra of other specimens, also containing ferrite, austenite, and sigma, are omitted for conciseness.

Supporting the XRD analysis, the optical microscopic images of the specimens, Figures 3a - j, show the evolution of the microstructure of SDSS SAF 2507 subjected to isothermal treatment at 900 °C for different times. Listed in Table 2 are the relative quantities of sigma and ferrite phases for each of the microscopic images. These percentages were determined using the ImageJ® software.

The amount of ferrite was double checked independently using the ferritescope, and the values obtained using both methodologies are plotted in Figure 4 for comparison. Both measurements confirm that there is a peak in the ferritic content from specimen S0 to S5. Neither of these specimens show sigma phase precipitates.

The specimen in the solubilized condition, S0, has its microstructure shown in Figure 3a, with a magnification of 1.000x. For this specimen, the grain boundaries are well defined, with the ferritic matrix in blue and the austenite islands in beige. There are no deleterious phases in this specimen, as demonstrated in the XRD spectrum, Figure 2a. Figure 3b shows the microstructure for a treatment time of 5 min. It is possible to visualize a predominantly ferritic and austenitic microstructure, with some traces of secondary austenite, possibly originated by rapid cooling after isothermal treatment at 900 °C³⁷. This precipitation of secondary austenite did not reduce the ferrite content; on the contrary, the ferritic matrix grew in specimen S5, as indicated in Table 2. Figure 3c shows the microstructure of specimen S15, subjected to 15 min of treatment. Here it is possible to see the secondary austenite present to an even greater extent in the ferritic matrix. In this microscopic image, it is possible to see some sigma precipitates in white building up in the ferrite-austenite interface. Figures 3d, e, and f show the sigma phase growing at the expense of the ferritic matrix for specimens S30 (1.2%), S45 (5.6%), and S60 (7.4%), respectively.

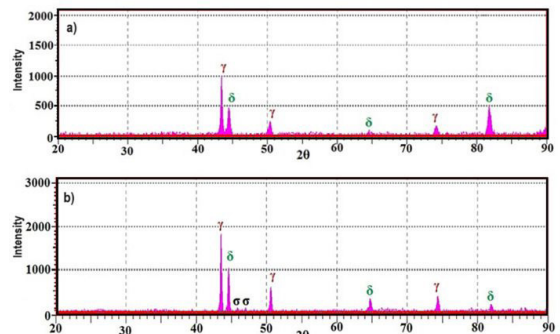


Figure 2. X-ray diffraction spectra for a) solubilized specimen S0, and b) specimen S30.

Table 2. Percentages of sigma and ferrite in each specimen.

Specimen	S0	S5	S15	S30	S45	S60	S90	S120	S150	S180
Sigma (%)	0.0	0.0	0.4	1.2	5.6	7.4	7.6	11.1	11.2	9.3
Ferrite (%)	48.1	50.4	36.9	33.4	29.9	26.5	29.8	24.6	22.7	24.9

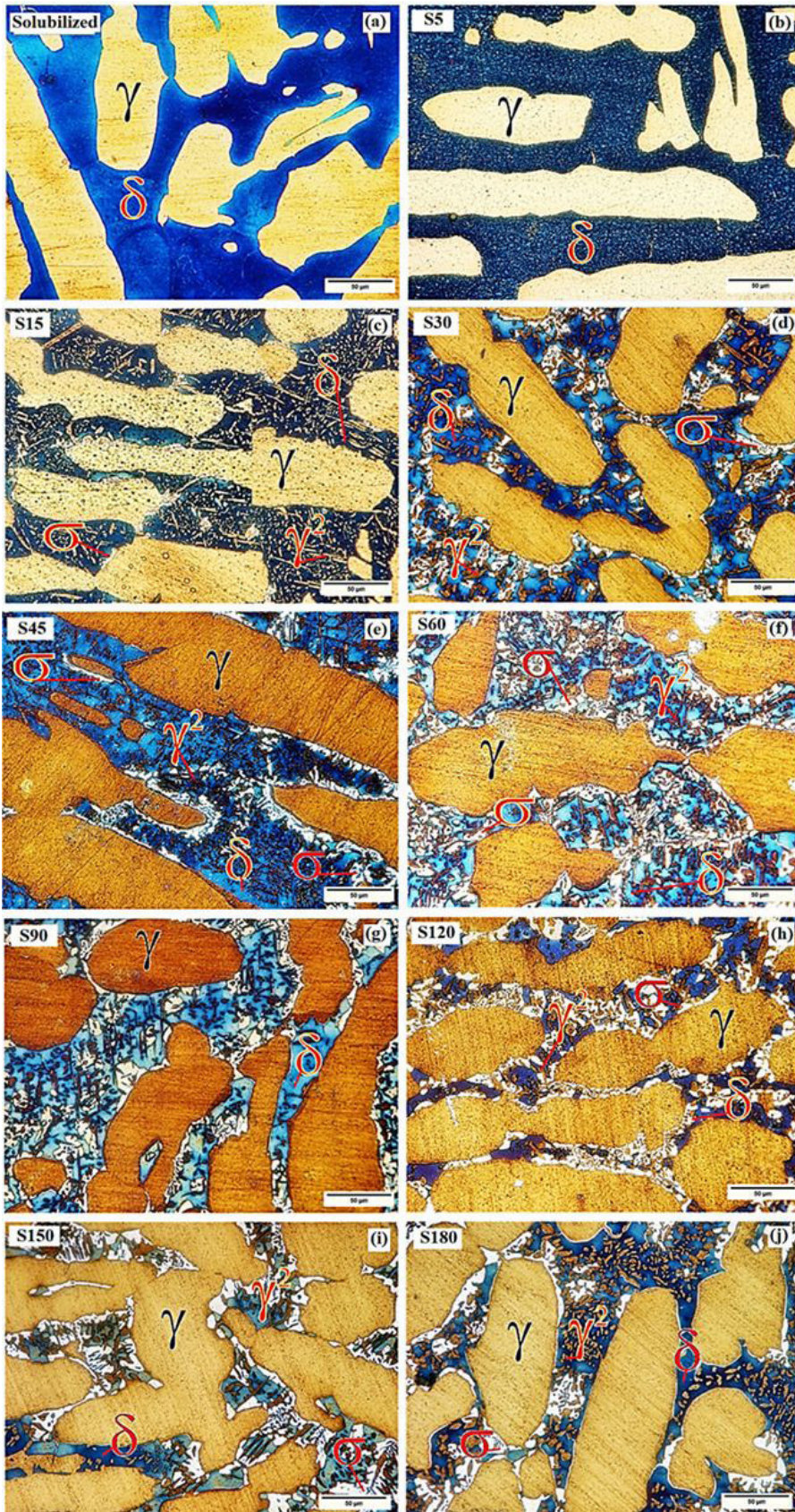


Figure 3. Metallurgical microscopic images of the specimens.

The microstructure of specimen S90 is shown in Figure 3g. This microstructure is characterized by a higher content of ferrite when compared with that of specimen S60, while the sigma phase percentage is nearly the same. Figures 3h and g show the microstructures of specimens S120 and S150, respectively. For these treatment times, the sigma phase grows even further, while secondary austenite decreases. ³⁷From specimen S150 to S180, the amount of sigma phase decreases, as shown in Table 2. This phenomenon signals the beginning of solubilization of the elements that are present in the material.

Figure 5 shows the SEM image of specimen S90, for which the thermal aging time was 90 min at 900 °C. In this image, each of the constituent phases are identified and all of them had their chemical composition analyzed by EDS. The sigma phase is visualized in SEM imaging through its backscattered electrons and appears in white in the microscopic image. The EDS graphs for each of the constituent phases

are shown schematically in Figures 5a–d and the chemical compositions for these phases are summarized in Table 3. The sigma phase has the highest Mo content (while Mo content lies in the range of 3.5% to 6.5% in the austenite and ferrite phases, it increases to about 9% in the sigma phase), which is characteristic of this secondary phase of DSS alloys. The EDS data for the secondary austenite phase show that its chemical composition is very similar to that of the primary austenite, which is expected since they have the same microstructure, even though they are formed through different reaction mechanisms. The austenitic grains grew larger near the regions in the ferrite phase with a higher Ni content due to isothermal aging and the formation of the sigma phase³⁷.

3.2. Ultrasonic attenuation analysis

The densities measured with the densimeter are listed in Table 4, along with each specimen's thickness.

Three ultrasonic measurements were taken for each specimen and their average values were registered. The parameters obtained from these measurements, i.e. longitudinal and shear velocity, are listed in Table 5. Figure 6 shows an A-scan, identifying the first and second peaks as A_0 and A_1 , respectively. The ratios A_0 / A_1 obtained in each experiment were used to calculate the attenuation coefficients.

The attenuation coefficient is dependent on the complexities of the microstructure, and is notably affected by grain size, interfacial phenomena, and the kinetics of the precipitation of the sigma phase and secondary austenite^{38–40}. As illustrated in Figure 7, the aging process induced microstructural changes that directly influenced the attenuation coefficient. Attenuation measurements begin to decay already in the sample treated for 5 min (S5), although slightly recovering in specimen S15. However, in specimen S30, in which there is a significant growth of the sigma phase, a substantial decrease in the attenuation signal is observed (approximately 0.30 dB/mm). Throughout the heat treatment, the lowest signal is recorded at 120 min (S120), coinciding with the peak of the sigma

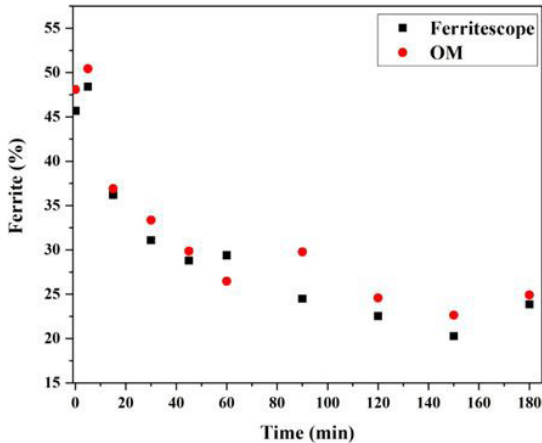


Figure 4. Percentage of ferrite in each specimen: ferritescope versus optical microscopy (OM).

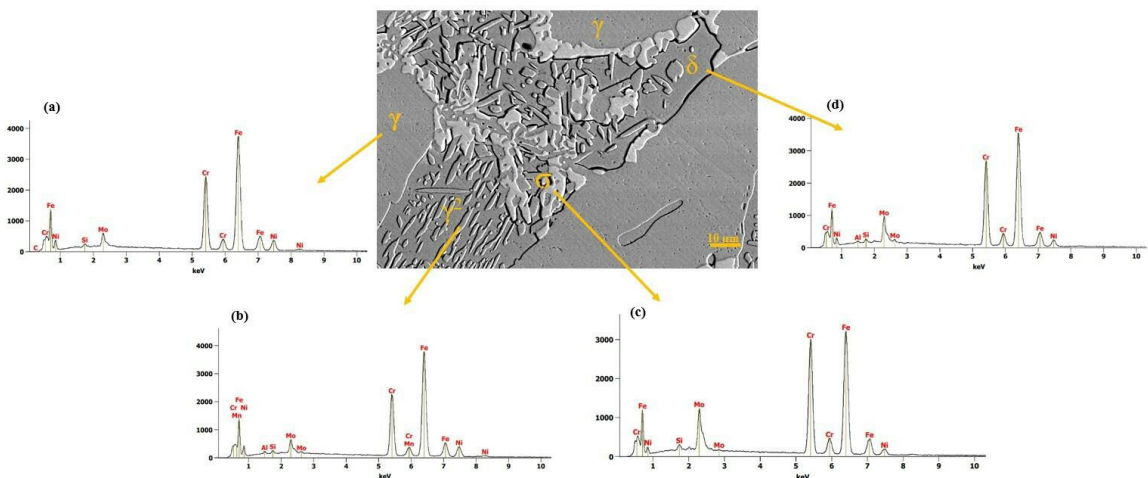


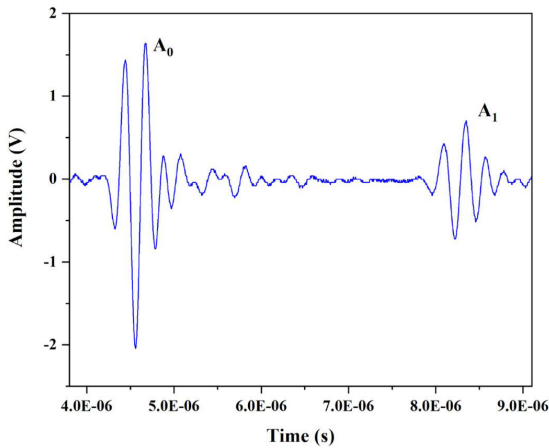
Figure 5. SEM imaging and energy dispersive spectrograms of specimen S90 with 1.000x magnification: a) austenite, b) secondary austenite, c) sigma, and d) ferrite.

Table 3. Phase compositions measured by EDS/SEM.

Element	Austenite (γ)	Ferrite (δ)	Secondary Austenite (γ^2)	Sigma (σ)
Fe	63.18% \pm 0.44%	60.81% \pm 0.44%	62.88% \pm 0.44%	54.85% \pm 0.43%
Cr	24.61% \pm 0.21%	27.92% \pm 0.23%	22.70% \pm 0.21%	31.62% \pm 0.24%
Ni	8.30% \pm 0.34%	4.27% \pm 0.30%	9.02% \pm 0.35%	3.87% \pm 0.29%
Mo	3.51% \pm 0.14%	6.46% \pm 0.16%	3.87% \pm 0.14%	9.14% \pm 0.17%
Si	0.38% \pm 0.03%	0.36% \pm 0.05%	0.34% \pm 0.05%	0.52% \pm 0.03%
C	0.01% \pm 0.00%	-	-	-
Al	-	0.19% \pm 0.03%	0.26% \pm 0.05%	-

Table 4. Densities and thicknesses of specimens.

Specimen	S0	S5	S15	S30	S45	S60	S90	S120	S150	S180
Density (g/cm ³)	7.75	7.73	7.76	7.74	7.73	7.75	7.76	7.75	7.74	7.78
Thickness (mm)	10.89	10.81	10.74	10.85	10.99	10.98	10.93	10.68	10.91	10.85

**Figure 6.** Example of an A-scan used to calculate attenuation. Windowed signal showing first and second backwall echoes.

phase (ca. 11%) and the lowest concentration of the ferrite phase (24.6%). From 120 min onward, there is a subtle increase in the signal, maintaining the recovery trend, as demonstrated in Figure 7.

In general, it was noted that during the process that consumes the ferritic matrix, the attenuation coefficient tends to decrease. This finding is in accordance with the results of another study that pointed out that attenuation decreases as aging time increases and the ferrite phase is depleted in DSS 2205⁴¹. However, the increase in attenuation from 120 min until 180 min may be explained by the previously mentioned increase in austenite grain size, which has also been reported in the literature⁴².

3.3. Determination of elastic moduli via ultrasonic testing and nanoindentation

The elastic moduli were determined using both the ultrasonic and nanoindentation experimental data points. The elastic moduli derived from the ultrasonic testing, the instrumented indentation and hardness measurements, and

Table 5. Longitudinal and shear acoustic velocities for each specimen.

Specimen	Longitudinal velocity (m/s)	Shear velocity (m/s)
S0	5,992.71	3,075.38
S5	5,981.58	2,955.95
S15	5,977.82	3,144.31
S30	5,930.78	3,185.24
S45	5,917.45	3,312.59
S60	5,956.52	3,198.38
S90	5,931.28	3,207.94
S120	5,878.94	3,205.37
S150	5,920.43	3,194.32
S180	6,037.14	3,193.33

the Poisson ratio of each specimen are listed in Table 6. The nanoindentation measurements and ultrasonic-derived elastic moduli were calculated within a 95% confidence interval.

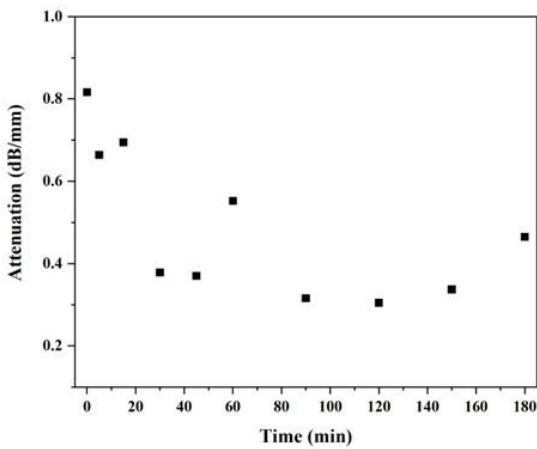
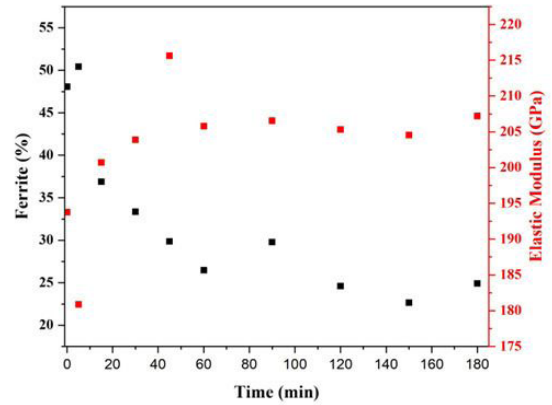
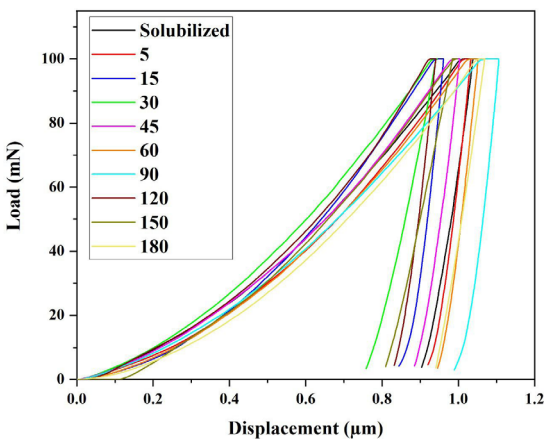
Some nanoindentation loading-unloading curves obtained experimentally are shown in Figure 8. The Poisson ratios found using the ultrasonic correlation ranged from 0.27 to 0.34, which is in accordance with the typical values for common metallic alloys⁴³.

The mean absolute error for the elastic modulus when these two methods are compared is 40.14 GPa, while the average of the elastic modulus is 202.43 GPa for the ultrasonic correlation and 235.01 GPa for the nanoindentation tests. The mean absolute error corresponds to 17.08% of the average value of the elastic modulus found using the nanoindenter, which is reasonably close to the values found employing the ultrasonic inspection, thus confirming the accuracy of this non-destructive technique for determining the elastic modulus of SAF 2507.

It is widely reported in the literature that even small amounts of sigma phase are enough to hamper mechanical properties of SDSS alloys, reducing their resistance while increasing localized hardness when present in volumetric contents above 10%⁴⁴. This dramatic effect of the sigma phase

Table 6. Poisson ratios, elastic moduli derived from ultrasonic testing (UT), indented elastic constants (EIT), and indented hardness (HIT).

Specimen	Poisson Ratio	UT Elastic Modulus (GPa)	EIT Elastic Modulus (GPa)	HIT Hardness (GPa)
S0	0.32	193.77 ± 46.09	260.65 ± 50.18	4.54 ± 0.52
S5	0.34	180.89 ± 22.52	251.95 ± 21.43	4.47 ± 0.13
S15	0.31	200.73 ± 6.97	250.21 ± 41.22	4.55 ± 0.35
S30	0.30	203.87 ± 9.79	217.74 ± 84.56	5.72 ± 1.10
S45	0.27	215.64 ± 1.41	238.26 ± 17.45	4.69 ± 0.15
S60	0.30	205.79 ± 6.54	252.17 ± 15.20	4.42 ± 0.17
S90	0.29	206.55 ± 4.79	229.17 ± 30.26	4.03 ± 0.17
S120	0.29	205.32 ± 10.15	238.89 ± 38.33	5.43 ± 0.42
S150	0.29	204.55 ± 3.66	166.72 ± 24.59	5.24 ± 0.66
S180	0.31	207.20 ± 14.14	244.35 ± 87.94	3.87 ± 0.35

**Figure 7.** Attenuation coefficients for different isothermal treatment times.**Figure 9.** Ferrite content versus the elastic modulus for each sample.**Figure 8.** Indentation curves from the nanoindentation tests.

on localized hardness, herein measured by a nanoindentation (last column of Table 6), is readily observed in the transition between specimens S90 and S120: when the sigma phase content goes from 7.6% (S90) to 11.1% (S120), the indented hardness jumps from around 4.0 GPa to approximately 5.4 GPa

(> 30% increase), which agrees with the previously reported observation that SDSS hardness is greatly magnified when the sigma content surpasses the 10% threshold.

It should also be noted that there are great variations in the elastic moduli for the nanoindentation measurements for each individual specimen. This is because the material is highly heterogeneous and has a complex and anisotropic microstructure. As the indenter tip is very small, it measures values that are accurate for the exact location where the measurement is taken but are not representative of the whole specimen. Because of that, several test runs were carried out for each specimen. The ultrasonic measurements, as noted before, were repeated three times for each specimen and there was some variation as well.

As previously mentioned, specimen S5 does not contain significant amounts of the sigma phase. Nevertheless, there is an increase in the content of ferrite in this specimen. Along with that, a decrease in the ultrasonic-derived elastic modulus was observed for this specimen when compared with the solubilized sample. During the initial stages of the eutectoid reaction that generates the sigma phase at the expense of the ferritic matrix ($\delta \rightarrow \sigma + \gamma^2$), the average values of the ultrasonic-derived elastic moduli slightly increased up to specimen S45, as can be seen in Figure 9. This may be attributed to the initial precipitation of the sigma phase, which hardens the material while reducing its tenacity, because it prevents the dislocations from moving freely⁴⁵.

The secondary austenite islands that first appear in specimen S15, and which keep nucleating and growing during the isothermal treatment (Figures 3a – j), are also a product of the same eutectoid decomposition of ferrite that generates the sigma phase. Therefore, in addition to the precipitation hardening effect caused by the formation of the sigma phase on the ferrite/austenite boundaries, the other mechanism which explains the increase in the elastic modulus even when the ferrite content drops from ca. 50% to ca. 30% – specimens S0 through S45 – is the grain boundary strengthening due to the increase in total grain boundaries originated by the formation of new grains of secondary austenite (γ^2 islands). These two mechanisms combined are enough to overcome the effect of the depletion of the ferrite phase (which has superior mechanical properties, including a higher elastic modulus, than those of austenite) and provoke an overall increase in the elastic modulus up until specimen S45.

The elastic modulus remains relatively stable after 45 min of thermal treatment and follows the same trend as the ferrite content – as one variable increases/decreases, so does the other accordingly, as can be seen in Figure 9 for specimens S60 to S180. This indicates that, from specimen S45 onwards, the combined effects of precipitation and grain boundary hardening are no longer relevant in determining the mechanical properties of the SAF 2507 specimens, with the ferrite content being the primary factor that dictates the behavior of the elastic constant. From specimen S60 to S180, this behavior changes, and, in general, a reduction in ferrite content resulted in a slight reduction of the elastic modulus. This trend in the elastic modulus for a heat treatment higher than 60 min closely aligns with those reported in another study⁴⁶.

For the SAF 2507 specimens studied in the current work, the sigma phase was barely present until 30 min of treatment time at 900 °C. After 30 min of isothermal treatment, there is a marked rise in the content of sigma, and the acoustic shear velocity tends to increase as the sigma phase builds up. As per the data listed in Table 5, longitudinal velocities remained fairly the same for all specimens regardless of treatment time, at around 5950 m/s. The most significant variations in sound propagation velocity were observed for the shear mode. As can be seen in Figure 10, the variations

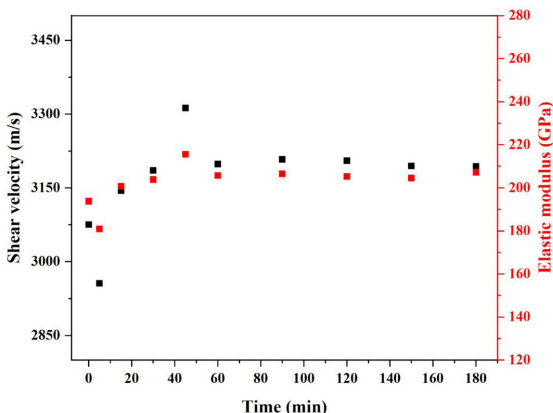


Figure 10. Ultrasonic-derived elastic modulus versus shear mode sound velocity.

of the ultrasonic-derived elastic modulus followed the same trend as those of the shear mode velocity. This indicates that this directionally dependent acoustic wave speed responds to microstructural changes that take place because of thermal treatment over time. This good correlation between shear velocity and elastic modulus is not unusual for ferrous materials – it has been demonstrated in another study that the elastic modulus of Fe and its metallic alloying elements has a stronger correlation with the shear mode velocity rather than with longitudinal velocity⁴⁷.

4. Conclusions

This experimental study on SAF 2507 SDSS subjected to thermal treatment at 900 °C for various aging times focused on characterizing microstructural evolution, phase changes, and mechanical properties. The findings are summarized as follows:

- X-ray diffraction confirmed the solubilization process and revealed distinct ferrite (δ) and austenite (γ) peaks, as well as peaks signaling the presence of the sigma (σ) phase, which emerged after 30 minutes of isothermal treatment, as shown by optical microscopy and SEM imaging.
- Ferrite content peaked from the solubilized state to 5 minutes of treatment, followed by sigma phase precipitation for higher aging times, because of the eutectoid decomposition of ferrite. Ultrasonic measurements indicated a decrease in attenuation during the process of depletion of the ferritic matrix.
- The elastic modulus increased as ferrite content decreased and sigma phase content increased, stabilizing after 45 minutes of treatment, which can be explained by the combined effects of precipitation hardening and grain boundary strengthening due to the buildup of the sigma phase in the ferrite/austenite borders and the nucleation of secondary austenite islands, respectively.
- Despite variations in nanoindentation measurements due to material heterogeneity, the averages of these values validate the ultrasonic measurements, which shows that these techniques are useful tools for studying SAF 2507 behavior under different heat treatment conditions.
- A strong correlation between shear mode velocity and elastic modulus was found which underscores the directional dependence of acoustic wave speeds in response to microstructural changes induced by thermal treatment.

These results provide valuable insights for optimizing SAF 2507 performance in practical applications, especially regarding manufacturing processes that involve thermal treatment at high temperatures, emphasizing the intricate interplay between microstructure, phase changes, and mechanical properties.

5. Acknowledgments

This work was carried out in the laboratories of the Federal Institute for Education, Science and Technology of Bahia, Salvador Campus. The authors also wish to thank Sandvik

and Anton Paar for their kindness in collaborating with this experimental study. Finally, we wish to thank the National Research Council of Brazil (CNPq) for granting scholarship support for the main author (Grant 132220/2023-7).

6. References

- Weisbrodt-Reisch A, Brummer M, Hadler B, Wolbank B, Werner EA. Influence of temperature, cold deformation and a constant mechanical load on the microstructural stability of a nitrogen alloyed duplex stainless steel. *Mater Sci Eng A*. 2006;416(1-2):1-10.
- Tan H, Jiang Y, Deng B, Sun T, Xu J, Li J. Effect of annealing temperature on the pitting corrosion resistance of super duplex stainless steel UNS S32750. *Mater Charact*. 2009;60(9):1049-54.
- Fellicia DM, Sutarsis, Kurniawan BA, Wulanari D, Purniawan A, Wibisono AT. Study of sigma phase in duplex SAF 2507. *IOP Conf Ser Mater Sci Eng*. 2017;202:012039.
- Sarlak H, Atapour M, Esmailzadeh M. Corrosion behavior of friction stir welded lean duplex stainless steel. *Mater Des* (1980-2015). 2015;66(Pt A):209-16.
- Ahn YS, Kang JP. Effect of aging treatments on microstructure and impact properties of tungsten substituted 2205 duplex stainless steel. *Mater Sci Technol*. 2000;16(4):382-8.
- Miranda-Pérez A, Rodríguez-Vargas B, Calliari I, Pezzato L. Corrosion Resistance of GMAW Duplex Stainless Steels Welds. *Materials* (Basel). 2023;16(5):1847.
- Gennari C, Pezzato L, Tarabotti G, Zambon A, Di Schino A, Calliari I. Influence of Electropulsing Treatments on Mechanical Properties of UNS S32750 Duplex Stainless Steel. *Materials* (Basel). 2020;13(7):1613.
- Wang L, Ding Y, Lu Q, Guo Z, Liu Y, Cui Z. Microstructure and corrosion behavior of welded joint between 2507 super duplex stainless steel and E690 low alloy steel. *Corrosion Communications*. 2023;11:1-11.
- Dobranszky J, Szabo PJ, Berecz T, Hrotko V, Portko M. Energy-dispersive spectroscopy and electron backscatter diffraction analysis of isothermally aged SAF 2507 type superduplex stainless steel. *Spectrochim Acta B At Spectrosc*. 2004;59(10-11):1781-8.
- Gunn R. Duplex stainless steels: microstructure, properties and applications. Sawston: Woodhead Publishing; 1997.
- Nilsson JO, Karlsson L, Andersson JO. Secondary austenite formation and its relation to pitting corrosion in duplex stainless steel weld metal. *Mater Sci Technol*. 1995;11(3):276-83.
- Sennour M, Jounneau PH, Esnouf C. TEM and EBSD investigation of continuous and discontinuous precipitation of CrN in nitrided pure Fe-Cr alloys. *J Mater Sci*. 2004;39(14):4521-31.
- Pérez AFM, Breda M, Calliari I, Medina GYP, Sandström R. Detrimental Cr-rich phases precipitation on SAF 2205 duplex stainless steels welds after heat treatment. *Soldag Insp*. 2016;21(2):165-71.
- Chan K, Tjong S. Effect of secondary phase precipitation on the corrosion behavior of duplex stainless steels. *Materials* (Basel). 2014;7(7):5268-304.
- Lopez N, Cid M, Puiggali M. Influence of α -phase on mechanical properties and corrosion resistance of duplex stainless steels. *Corros Sci*. 1999;41(8):1615-31.
- Michalska J, Sozańska M. Qualitative and quantitative analysis of σ and γ phases in 2205 duplex stainless steel. *Mater Charact*. 2006;56(4-5):355-62.
- Tavares SSM, Pardal JM, Ponzio E, Loureiro A, de Souza JA. Influence of microstructure on the corrosion resistance of hyperduplex stainless steel. *Materials and Corrosion*. 2010;61(4):313-7.
- Birks AS, Green RE, McIntire P. Ultrasonic testing. In: Birks AS, Green RE, McIntire P. *Non-destructive testing handbook*. 2nd ed. Columbus: American Society for Nondestructive Testing; 1991. p. 40-9.
- Kino GS. Acoustic waves. In: Kino GS. *Devices, imaging, and analog signal processing*. Upper Saddle River: Prentice Hall; 1986. p. 90-9.
- Wu SJ, Chin PC, Liu H. Measurement of elastic properties of brittle materials by ultrasonic and indentation methods. *Appl Sci* (Basel). 2019;9(10):2067.
- Auld BA. *Acoustic fields and waves in solids*. Hoboken: John Wiley & Sons; 1990.
- Szabo TL, Wu J. A model for longitudinal and shear wave propagation in viscoelastic media. *J Acoust Soc Am*. 2000;107(5):2437-46.
- Pandey DK, Pandey S. Ultrasonics: a technique of material characterization. In: Dissanayake D. *Acoustic waves*. Croatia: Sciyo; 2010. p. 397-430.
- Gallo M, Ferrara L, Naviglio D. Application of ultrasound in food science and technology: a perspective. *Foods*. 2018;7(10):164.
- Ahn B, Lee SS. Effect of microstructure of low carbon steels on ultrasonic attenuation. *IEEE Trans Ultrason Ferroelectr Freq Control*. 2000;47(3):620-9.
- Stella J, Cerezo J, Rodríguez E. Characterization of the sensitization degree in the AISI 304 stainless steel using spectral analysis and conventional ultrasonic techniques. *NDT Int*. 2009;42(4):267-74.
- Kittel C. *Introduction to solid state physics*. 8th ed. Hoboken: John Wiley & Sons; 2004.
- Guy AG. *Physical metallurgy for engineers*. 3rd ed. Boston: Addison Wesley Publishing Company INC; 1974.
- Edelmann X. Application of ultrasonic testing techniques on austenitic welds for fabrication and in-service inspection. *NDT Int*. 1981;14(3):125-33.
- Gibson JSKL, Schröders S, Zehnder C, Korte-Kerzel S. On extracting mechanical properties from nanoindentation at temperatures up to 1000 °C. *Extreme Mech Lett*. 2017;17:43-9.
- Oliver WC, Pharr GM. Measurement of hardness and elastic modulus by instrumented indentation: advances in understanding and refinements to methodology. *J Mater Res*. 2004;19(1):3-20.
- Cheng YT, Cheng CM. Scaling approach to conical indentation in elastic-plastic solids with work hardening. *J Appl Phys*. 1998;84(3):1284-91.
- Yan FK, Zhang BB, Wang HT, Tao NR, Lu K. Nanoindentation characterization of nano-twinned grains in an austenitic stainless steel. *Ser Mater*. 2016;112:19-22.
- Pharr GM, Bolshakov A. Understanding nanoindentation unloading curves. *J Mater Res*. 2002;17(10):2660-71.
- Fedorov A, Zhitenev A, Strelakovskaya D, Kur A. Quantitative description of the microstructure of duplex stainless steels using selective etching. In: *The 1st International Electronic Conference on Metallurgy and Metals; 2021; Basel, Switzerland*. Proceedings. Basel, Switzerland: MDPI; 2021. p. 4.
- Kinsler LE, Frey AR, Coppens AB, Sanders JV. *Fundamentals of acoustics*. 4th ed. Hoboken: John Wiley & Sons; 2000.
- Nilsson JO, Karlsson L, Andersson JO. Secondary austenite formation and its relation to pitting corrosion in duplex stainless steel weld metal. *Mater Sci Technol*. 1995;11(3):276-83.
- Gruttadauria A, Barella S, Mapelli C, Mombelli D. Influence of Different Soaking Times at 1050 °C on the UT Response Due to Microstructure Evolution of 2205 Duplex Stainless Steel. *Metals* (Basel). 2020;10(4):503.
- Renaud A, Tie B, Mouronval AS, Schmitt JH. Multi-parameter optimization of attenuation data for characterizing grain size distributions and application to bimodal microstructures. *Ultrasonics*. 2021;115:106425.
- Norouzian M, Islam S, Turner JA. Influence of microstructural grain-size distribution on ultrasonic scattering. *Ultrasonics*. 2020;102:106032.

41. Ruiz A, Ortiz N, Carreón H, Rubio C. Utilization of ultrasonic measurements for determining the variations in microstructure of thermally degraded 2205 duplex stainless steel. *J Nondestr Eval.* 2009;28(3-4):131-9.
42. Vijayalakshmi K, Muthupandi V, Jayachitra R. Influence of heat treatment on the microstructure, ultrasonic attenuation and hardness of SAF 2205 duplex stainless steel. *Mater Sci Eng A.* 2011;529:447-51.
43. Hassan KR, Alam MS, Basit M, Suhling JC, Lall P. Experimental characterization of the dependence of the poisson's ratio of lead free solder on temperature, strain rate, solidification profile, and isothermal aging. In: 2019 18th IEEE Intersociety Conference on Thermal and Thermomechanical Phenomena in Electronic Systems (ITherm); 2019; USA. Proceedings. USA: IEEE; 2019. p. 1342-53.
44. Tavares SSM, Pardal JM, Almeida BB, Mendes MT, Freire JLF, Vidal AC. Failure of superduplex stainless steel flange due to inadequate microstructure and fabrication process. *Eng Fail Anal.* 2018;84:1-10.
45. Wang R. Precipitation of sigma phase in duplex stainless steel and recent development on its detection by electrochemical potentiokinetic reactivation: a review. *Corrosion Communications.* 2021;2:41-54.
46. Li S, Wang Y, Wang X. Effects of ferrite content on the mechanical properties of thermal aged duplex stainless steels. *Mater Sci Eng A.* 2015;625:186-93.
47. Doghmane M, Hadjoub F, Doghmane A, Hadjoub Z. Approaches for evaluating Young's and shear moduli in terms of a single SAW velocity via the SAM technique. *Mater Lett.* 2007;61(3):813-6.